

Article

Tuning the Morphology of ZnO Nanostructures with the Ultrasonic Spray Pyrolysis Process

Elif Emil ^{1,2}, Gözde Alkan ^{3,*}, Sebahattin Gurmen ¹, Rebeka Rudolf ⁴ , Darja Jenko ⁵ 
and Bernd Friedrich ³ 

¹ Department of Metallurgical & Materials Eng., Istanbul Technical University, 34469 Istanbul, Turkey; emil.elif@gmail.com (E.E.); gurmen@itu.edu.tr (S.G.)

² Department of Materials Science & Tech., Turkish-German University, 34820 Istanbul, Turkey

³ IME Institute of Process Metallurgy and Metal Recycling, RWTH Aachen University, Intzestrasse 3, 52056 Aachen, Germany; bfriedrich@ime-aachen.de

⁴ Faculty of Mechanical Engineering, University of Maribor, Smetanova ulica 17, 2000 Maribor, Slovenia; rebeka.rudolf@um.si

⁵ Institute of Metals and Technology, Laboratory of Applied Surface Science, Lepi pot 11, SI-1000 Ljubljana, Slovenia; darja.jenko@imt.si

* Correspondence: galkan@ime-aachen.de; Tel.: +49-241-95873

Received: 6 June 2018; Accepted: 19 July 2018; Published: 24 July 2018



Abstract: Nanostructured zinc oxide (ZnO) particles were synthesized by the one step Ultrasonic Spray Pyrolysis (USP) process from nitrate salt solution ($\text{Zn}(\text{NO}_3)_2 \cdot 6\text{H}_2\text{O}$). Various influential parameters, from $\text{Zn}(\text{NO}_3)_2 \cdot 6\text{H}_2\text{O}$ concentrations (0.01875–0.0375 M) in the initial solution, carrier gas (N_2) flow rates (0.5–0.75 L/min) to reaction temperature (400–800 °C), were tested to investigate their role on the final ZnO particles' morphology. For this purpose, Scanning Electron Microscopy (SEM), High Resolution Transmission Electron Microscopy (HRTEM) and (Selected Area Electron Diffraction) SAED techniques were used to gain insight into how the ZnO morphology is dependent on the USP process. It was revealed that, by certain parameter selection, different ZnO morphology could be achieved, from spherical to sphere-like structures assembled by interwoven nanoplate and nanoplate ZnO particles. Further, a more detailed crystallographic investigation was performed by XRD and Williamson-Hall (W-H) analysis on the ZnO with unique and non-typical planar morphology that was not reported before by USP synthesis. Moreover, for the first time, a flexible USP formation model was proposed, ending up in various ZnO morphologies rather than only ideal spheres, which is highly promising to target a wide application area.

Keywords: ZnO; ultrasonic spray pyrolysis; influential parameters; formation mechanism; structure; morphologies; characterization; TEM; HRTEM

1. Introduction

ZnO in a nanosized form is an indispensable candidate for electronic, optical, and gas sensors, as well as in catalysis applications, owing to its band gap value of 3.37 eV, large exciton binding energy of 60 meV and high electron mobility [1–5]. In the last decade, ZnO with various morphologies, including flower-like [6,7], nanodisc [1], nanobelt [8], and nanotube [9], targeting various application areas, have been investigated using different synthesis methods, e.g., sol-gel [10], hydrothermal [11], the microwave-assisted method [12] and spray pyrolysis [13]. Kajbafvala et al. reported synthesis of spherical and flower-like ZnO via the microwave-assisted method for organic dye photo-degradation via UV lamp irradiation. It was revealed that the degradation efficiency of the spherical particles is better than that of those with flower-like morphology due to their higher surface area, which provides

the absorption of oxygen molecules and OH⁻ ions, resulting in an increment of H₂O₂ and OH⁻ radicals' formation rate [14]. In another study, Sin et al. [15] reported synthesised self-assembled ZnO microsphere formed by nanoplanar crystal units to improve photocatalytic performance for various endocrine-disrupting chemicals under UV irradiation by the chemical solution route. The enhancement in the photocatalytic performance was attributed to the combined effects of the hierarchical surface structure and the large surface area, which suppresses the recombination of photo-generated electrons (e⁻) and holes (h⁺), and expedites the diffusion of electrons [15]. In another study by Li et al., carbon-doped and coated spherical ZnO particles were synthesized for use as anode material in high power Zn-Ni batteries. ZnO microspheres exhibit excellent cycling stability and superior high-rate performance [16].

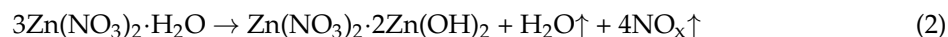
These previous studies revealed that ZnO finds wide application areas, e.g., planar nano ZnO favors catalytic properties owing to its higher surface area, while granular nano ZnO is preferred in optical applications due to better absorption behavior, and battery applications due to structural stability and anti-corrosion capability [13]. Considering these morphology dependent utilizations of ZnO, adjusting a synthesis method to end up with varying morphologies in a controlled way would be advantageous. There have already been some studies reported, that control ZnO morphology by wet chemical methods is possible; however, these used reactant agents, such as polyethylene glycol (PEG) and cetyltrimethylammonium bromide (CTAB). In our previous study focusing on Ag/ZnO core shell nanostructured materials for photocatalytic applications, under some synthesis conditions, variation from the typical spherical morphology Ultrasonic Spray Pyrolysis (USP) into entangled plates was observed in ZnO particles without any additives [17]. These findings raised the question of whether it is possible to tune ZnO particles morphology by the USP process with simplicity, good process control, high flexibility, and good scale-up potential, without any additives, obtaining high-purity products [17]. For this purpose, varying influential USP process parameters like Zn(NO₃)₂·6H₂O concentration in the initial solution, carrier gas (N₂) flow rate and reaction temperature (400–800 °C) were examined. Based on this, the aim was to synthesize ZnO nanoparticles and to investigate the newly formatted ZnO morphology through the USP process. With detailed ZnO morphological investigations by High Resolution Transmission Electron Microscopy (HRTEM) and Scanning Electron Microscopy (SEM), the role of each USP parameter was determined. A more detailed crystallographic investigation was performed via XRD and W-H analysis only on the non-conventional nanostructured ZnO particles. Moreover, the reason behind the different morphologies of ZnO were explained, and a reaction progress model was proposed considering the USP process and thermodynamic conditions. There has been no study in the literature utilizing USP to synthesize ZnO nanoparticles with the aim of obtaining different morphologies.

2. Experimental Procedures

2.1. Synthesis of Zinc Oxide Particles

For the synthesizing of ZnO particles with USP, an aqueous solution of zinc nitrate hexahydrate (Zn(NO₃)₂·6H₂O, purity > 99.9%) was used, purchased from MERCK Chemical GmbH (Darmstadt, Germany) Zinc nitrate hexahydrate, at the determined amount given in Table 1, was dissolved in distilled water and stirred for 30 min by a magnetic stirrer. This solution represents the so-called precursor, which was atomized by an ultrasonic nebulizer at 1.7 MHz. The formed aerosol was transferred into a one-step USP device to the pre-heated furnace (Nabertherm, R 50/250/12, Lilienthal, Germany) through a quartz tube (0.7 m length and 0.02 m diameter) using N₂ gas. The experiments were conducted with 0.5 L/min and 0.75 L/min N₂ flow rate at 400, 600 and 800 °C reaction temperature for 3 h. The thermal decomposition of Zn(NO₃)₂·6H₂O under air atmosphere during the spray pyrolysis has been reported previously [17,18]. The chemical balance equations were given in 3 reaction steps:





ZnO is the final product of all intermediate product decomposition of zinc nitrate. Synthesized ZnO particles were collected in a washing bottle filled with ethanol. Details of the synthesis procedure can be found elsewhere [19,20]. To characterize nanostructured ZnO particles, ethanol was evaporated in a drying oven at 70 °C for 300 s. A summary of the process parameters is illustrated in Table 1.

Table 1. Process parameters of nanostructured ZnO particles synthesized with various solution concentrations, reaction temperature and N₂ gas flow rate.

Sample Name	Zn(NO ₃) ₂ ·6H ₂ O Concentration (mol/L)	Reaction Temperature (°C)	N ₂ Gas Flow Rate (L/min)
S1	0.01875	800	0.5
S2	0.02875	800	0.5
S3	0.03750	800	0.5
S4	0.02875	600	0.5
S5	0.02875	400	0.75
S6	0.02875	600	0.75
S7	0.02875	800	0.75

2.2. Characterization of Zinc Oxide Particles

The morphology of the ZnO nanoparticles (size and shape) was examined by Field Emission Scanning Electron Microscopy (FE-SEM, JSM 700F, JEOL, Tokyo, Japan), operating at 5 kV. During SEM sample preparation, the SEM holder was grinded, the particles were dispersed in ethanol, and then the suspension was added dropwise onto the SEM holders, and, afterwards, a conductivity Pt coating was added to prevent charging of the particles by Sputter Coater (Polaron Range SC7620, Quorum Technologies, East Sussex, UK). A Transmission Electron Microscope (TEM, JEM-2100 HR, JEOL, Tokyo, Japan) with integrated Selected Area Electron Diffraction (SAED) pattern analysis, operating at 200 kV was used. Samples of ZnO nanoparticles in demineralized water for TEM analyses were drop cast onto a copper TEM grid covered with a carbon support film, dried, and then used for investigations.

The as-synthesized ZnO nanoparticles were analyzed using a X-ray diffractometer operating at 40 mA and 40 kV with Cu-K α radiation ($\lambda = 0.154051$ nm). The diffraction spectra were recorded 2θ in the range between 10° and 90° in 2θ steps of 0.02 degrees. Phase composition was determined with a digital library of crystallographic cards JCPDS. Based on the Full Width at Half Maximum (FWHM), zinc oxide crystallite size was evaluated by Williamson–Hall (W-H) analysis and the Debye-Scherrer (DS) method.

3. Results and Discussion

3.1. Effect of Precursor Concentration

SEM micrographs of nanostructured ZnO particles are given in Figure 1, revealing the effect of precursor concentration on final morphology.

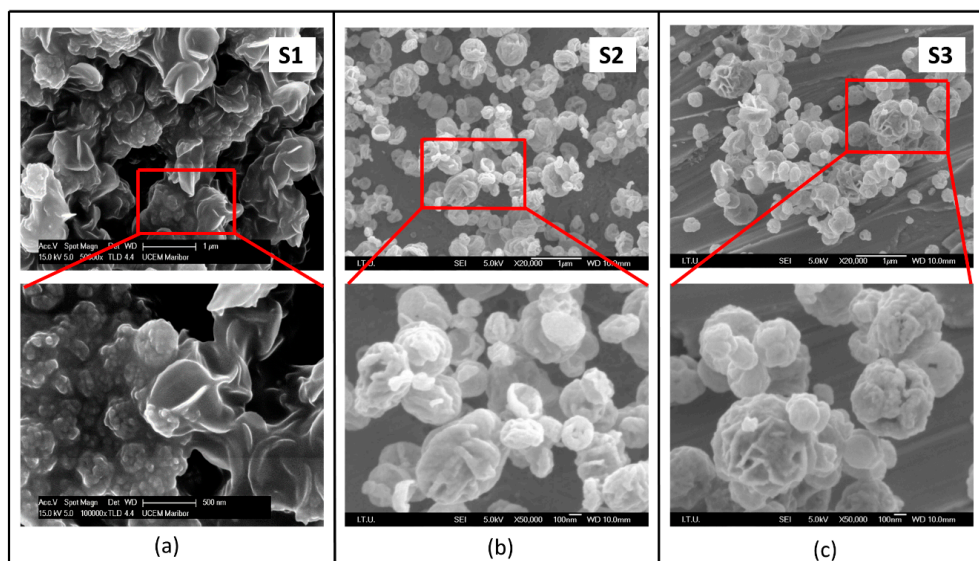


Figure 1. SEM micrographs of nanostructured ZnO particles (a) S1; (b) S2; and (c) S3, at 800 °C, 0.5 L/min of N₂ gas flow rate.

As can be observed, a relatively lower zinc nitrate concentration (0.01875 mol/L) exhibited dominant plates and accompanying sphere-like morphology, assembled by interwoven nanoplates, which is not commonly achieved via USP. A gradual change in the microstructure was revealed by increases in zinc nitrate concentrations. An increase to 0.02875 mol/L resulted in a sphere-like morphology assembled by nanoplates. A further increase to (0.03750 mol/L) resulted in dominant granular accompanied particles. Although there are many studies dealing with ZnO synthesis with USP, such a unique morphology has not been reported and explained previously. In order to better understand its crystallography and to see if this morphology difference was due to a different phase formation, a detailed crystallographic investigation was performed only on that sample. The corresponding XRD pattern is given in Figure 2.

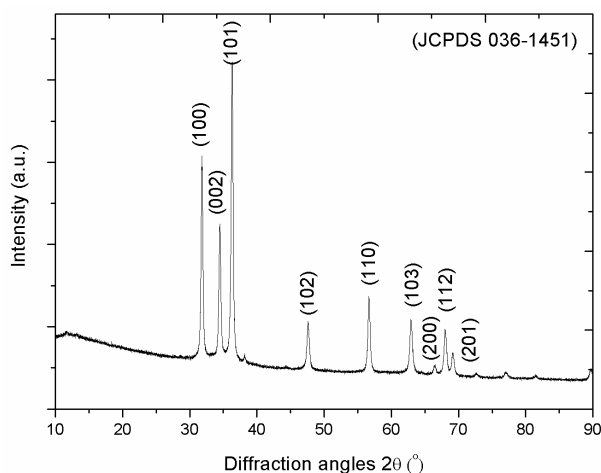


Figure 2. Indexed XRD pattern of sample S1.

As shown in Figure 2, reference sample S1 exhibited a phase pure zinc oxide hexagonal structure with a space group P63mc (186), unit cell of $a = 3.2533 \text{ \AA}$ and $c = 5.2073 \text{ \AA}$ corresponding to JCPDS Card 00-036-1451. The peaks at $2\theta = 31.80^\circ, 34.45^\circ, 36.32^\circ, 47.56^\circ, 56.65^\circ, 62.89^\circ, 66.38^\circ, 67.98^\circ$ and 69.10° are assigned to (100), (002), (101), (102), (110), (103), (200), (112) and (201) diffraction planes,

respectively. No characteristic peaks of zinc nitrate salt were detected in the diffraction pattern, implying termination of decomposition reaction. Based on the most intense peaks (101) diffraction planes, the crystallite size was calculated using the DS method, where the contribution of crystallite size and lattice strain to total peak broadening were not considered. The β parameter was corrected due to the effect of instrumental broadening on total peak broadening in DS, and the crystallite size of S1 was calculated as 24 nm by DS. However, the contribution of lattice strain on total peak broadening should be noted, since lattice strain is induced by a rapid heating/cooling rate and short residence time of the USP process, as reported previously [21]. This relation is expressed in Equation (4):

$$\beta_{hkl} = \beta_D + \beta_s \quad (4)$$

Williamson Hall (W-H) analysis was preferred to evaluate the crystallite size and lattice strain. Details of the W-H analysis are explained elsewhere [22]. The intense peaks corresponding to (100), (002), (101), (102), (110), (103) and (112) planes were selected to conduct the W-H analysis. The strain-induced broadening was connected with crystal distortion, and is defined in Equation (5):

$$\varepsilon \approx \beta_s / \tan \theta \quad (5)$$

DS relation, Equation (4), can be reformulated with Equation (5) which results in Equation (6):

$$\beta_{hkl} \cos \theta = (k\lambda/D) + (4\varepsilon \sin \theta) \quad (6)$$

where β_{hkl} is the total peak broadening, k is the shape factor, λ is the wavelength of Cu-K α radiation ($\lambda = 0.154051$ nm), D is the crystallite size of the synthesized particles, ε is the lattice strain, β is FWHM of the peak, and θ are the Bragg angles. The individual contribution of crystallite size and lattice strain were evaluated by the W-H method integrated with Uniform Deformation Model (UDM). Graphics of $(4\varepsilon \sin \theta)$ versus $\beta_{hkl} \cos \theta$ were drawn in Figure 3. Crystallite size and lattice strain respectively were estimated from the intercept on the y-axis and slope of linearly fitted data.

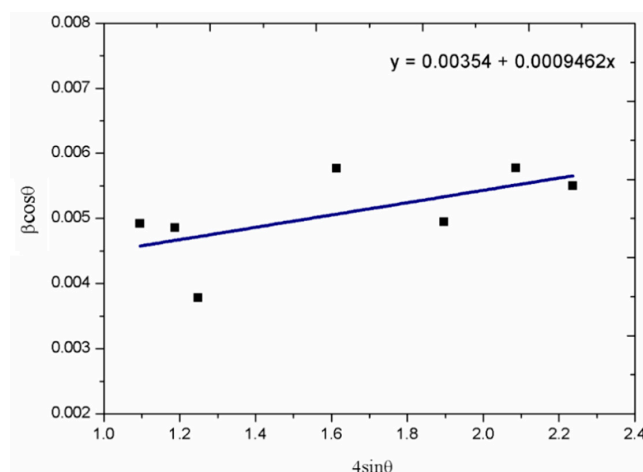


Figure 3. Williamson-Hall (W-H) analysis integrated with Uniform Deformation Model (UDM) model of S1.

Based on the broadening X-ray diffraction peak (FWHM), the crystallite sizes of the synthesized particles from 0.01875 mol/L were estimated at 38 nm and 24 nm using the W-H method integrated with UDM, and the DS method, respectively. This fine crystallite size and the XRD pattern given in Figure 2, which is consistent with the literature, imply the formation of secondary particles by coalescence of these primary crystals. Due to the neglect of the intrinsic strain at the lattice, the values of the crystallite sizes calculated using the W-H method differed from that evaluated by DS analysis, as expected. According to the plots of $(4\varepsilon \sin \theta)$ vs. $\beta_{hkl} \cos \theta$ of particles, the intrinsic strain at the lattice

for S1 was found to be 9.462×10^{-4} . It was proved that DS analysis calculates a smaller crystallite size than the size calculated using the W-H method in the presence of a tensile lattice strain. Moreover, these strain and crystallite size values were found to be similar to values reported previously for spherical ZnO particles [23,24]. Since the crystallographic findings do not differ dramatically from the previously reported data for spherical ZnO, the origin of this unique morphology was searched for in the USP formation mechanism.

In order to highlight microstructural features in detail, HRTEM was performed on the samples synthesized from varying precursor concentrations. Corresponding HRTEM images with electron diffraction patterns can be found in Figure 4.

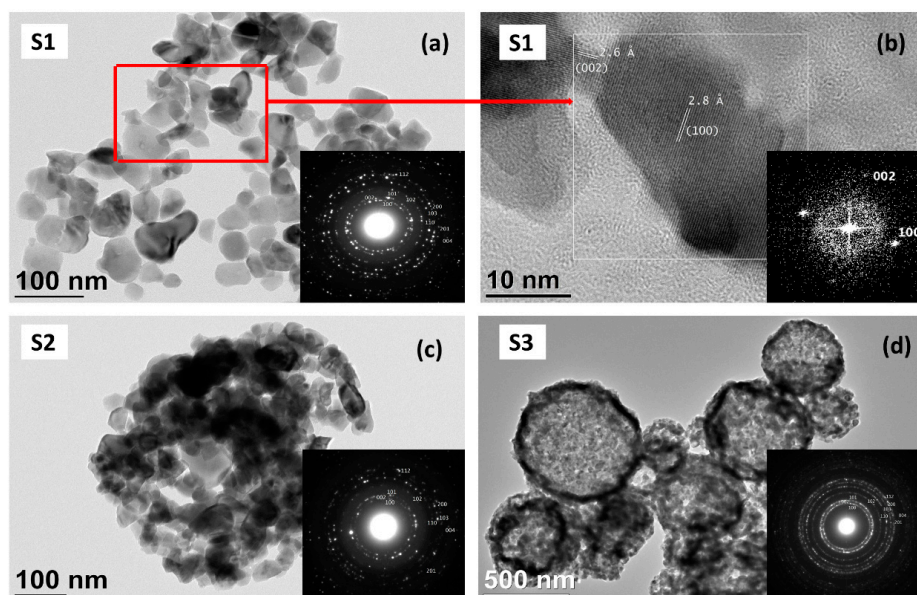


Figure 4. High Resolution Transmission Electron Microscopy (HRTEM) micrographs and electron diffraction ring pattern of S1 (a); HR-TEM micrographs and electron diffraction spot pattern S1 (b); HRTEM micrographs and electron diffraction ring pattern of S2 (c) and S3 (d).

The TEM Bright-Field (BF) image, and the corresponding Selected Area Electron Diffraction (SAED) pattern of S1 solution concentration, showed fine particle sizes in the range of 10–70 nm. The planar morphology was also revealed, and even some hexagonal particles were observed. The HR-TEM image (Figure 2b), with a 2-D Fast Fourier Transform (FFT), shows a lattice of two ZnO nanoparticles synthesized from 0.01875 mol/L. The bigger particle is oriented in the (100) direction, and the attached neighboring particle on the left of this particle is oriented in the (002) direction. The measured distance from the HR-TEM image between the lattice planes is 2.8 Å in the (100) direction and 2.6 Å in the (002) direction, which is in very good agreement with the cell parameters of ZnO (cell parameters $a = 3.2498 \text{ \AA}$, $c = 5.2066 \text{ \AA}$). In parallel with the XRD findings, with an increase in concentration, a gradual change in morphology was observed in the HRTEM images. Planar fine crystals were transformed into spherical ZnO nanostructured spheres (500–700 nm) with increasing concentrations. The SAED of all ZnO nanoparticles showed characteristic diffraction of a ring pattern, with some brighter and more distinct spots in the rings, which indicated the presence of some larger crystallites, though the rings were still relatively continuous, which meant that the crystallites were small, in the nm range, and in a random orientation. The electron diffraction spots can be described by a hexagonal crystalline-structured zinc oxide with a space group P63mc (JCPDS card No. 00-00-036-1451) with indices as shown in the inset of Figure 4a and in accordance with the XRD spectrum in Figure 2. Although the microstructure changed from planar to spherical with increasing solution concentrations, they exhibited the same crystallite structure [23]. In previous

studies, it was reported that the decomposition of zinc nitrate hexahydrate into zinc oxide takes place via step-wise reaction with the formation of a $Zn(NO_3)_2 \cdot 2Zn(OH)_2$ intermediate compound. However, before the decomposition takes place, the initial salts melt and reaction takes place in the liquid phase [17,18]. Since particle formation in the melt phase is driven by nucleation and growth processes, the final morphology can be adjusted by controlling nucleation and growth rates via process parameters. The different morphologies achieved in this study at various temperatures, concentrations, and flow rates can be explained by this fact.

In the case of a higher precursor concentration, supersaturation induces higher nuclei rates, yielding more nuclei formation and less growth rate, and resulting in the formation of spherical-like ZnO particles. Similarly, when the temperature increased, the supersaturation degree increased again. This also increased the nucleation rate and, therefore, at 800 °C, almost all samples exhibited spherical-like morphologies. In the USP process, temperature change and flow rate also act parallel to concentration in terms of supersaturation degree. Increased temperatures and flow rate results in higher temperature gradients and increases the supersaturation rate. In order to demonstrate the change, the supersaturation degree plays a crucial role in the final morphology; the optimal concentration (0.02875 mol/L) was selected and the temperatures and flow rates were varied to observe their individual effects.

3.2. Effect of Reaction Temperature and N_2 Gas Flow Rate

USP reaction temperature and gas flow rate together determine the residence time of droplets/particles in the heating zone, and therefore they also play a significant role in the nucleation step and growth mechanism. In previous synthesis conditions, reaction temperature was fixed at 800 °C. Temperature was changed to 600 °C/400 °C while ensuring complete decomposition of zinc nitrate. SEM micrographs of the formed ZnO particles can be found in Figure 5.

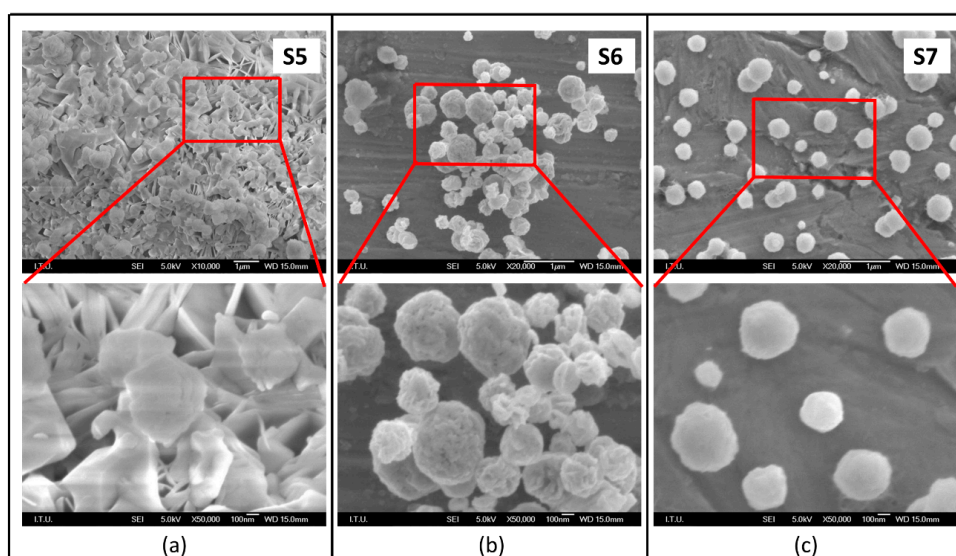


Figure 5. SEM micrographs of nanostructured ZnO particles synthesized at various reaction temperatures at S5 (a), S6 (b) and S7 (c), where concentration (0.02875 mol/L) and flow rate (0.5 L/min) were constant.

To begin with, it is worth emphasizing that all samples synthesized at different temperatures exhibited complete conversion to ZnO. With increasing synthesis temperature, similar to the change in concentration, a gradual morphological change was observed from plates to spheres. When the reaction temperature was high, the supersaturation rate and mobility of particles were expected to be high. Higher supersaturation degree yielded higher nucleation rates, while a higher mobility increased

the collision rates and growth rates of individual particles. For low temperatures, the driving force of the reaction in the system and nucleation rates are low. Therefore, there can be an accumulation on already existing nuclei and directed growth may be observed, as shown in Figure 5, in parallel with low precursor concentrations (see Figure 1a). However, when a particle synthesized at the highest temperature was considered, there was no observed coarsening, which implies that the increased nucleation rate was more dominant.

In order to assess flow rate effect in morphology, a high temperature (800 °C) was used to ensure complete conversion and ZnO was synthesized at a relatively lower flow rate. The SEM micrographs presented in Figure 6 reveal the effect of flow rate.

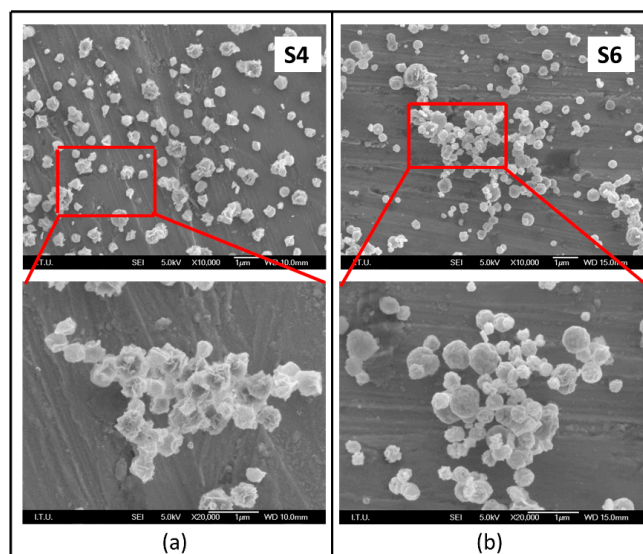


Figure 6. SEM micrographs of nanostructured ZnO particles synthesised from 0.02875 mol/L at 600 °C; (a) 0.75 L/min N₂ gas flow and (b) 0.5 L/min N₂ gas flow rate.

Figure 6 reveals that an obvious morphology change occurred when the flow rate was varied. Although the particle size remained similar, when the flow rate decreased from 0.75 to 0.5 L/min, the granular morphology was replaced with plates and spheres assembled by these plates. In the case of higher flow rates, a higher gradual temperature was achieved within the droplet, which also increased the supersaturation and driving force of the reaction.

3.3. Formation Mechanism

In the USP process, the aerosol droplets undergo evaporation/drying, precipitation and thermolysis in a single-step process and under extreme synthesis conditions (high droplet/particle heating rate and high surface reaction), as presented in Figure 7. Within the short reaction time (2–3 s), intraparticle transport, solute nucleation and growth take place. The morphological findings presented in Figures 1, 5 and 6, revealing the effect of temperature, precursor concentration and flow rate, are consistent, implying that lower supersaturation degrees decrease the driving force of the reaction and, hence, nucleation rates. During the USP process, as summarized in Figure 7, in the case of lower nucleation rates, growth occurs from already existing nuclei in favored crystallographic directions, ending up with planar growth. In the case of a higher driving force, higher nucleation rates ensure homogenous nucleation, and precipitation takes place in the determined volume and shape of spherical droplets.

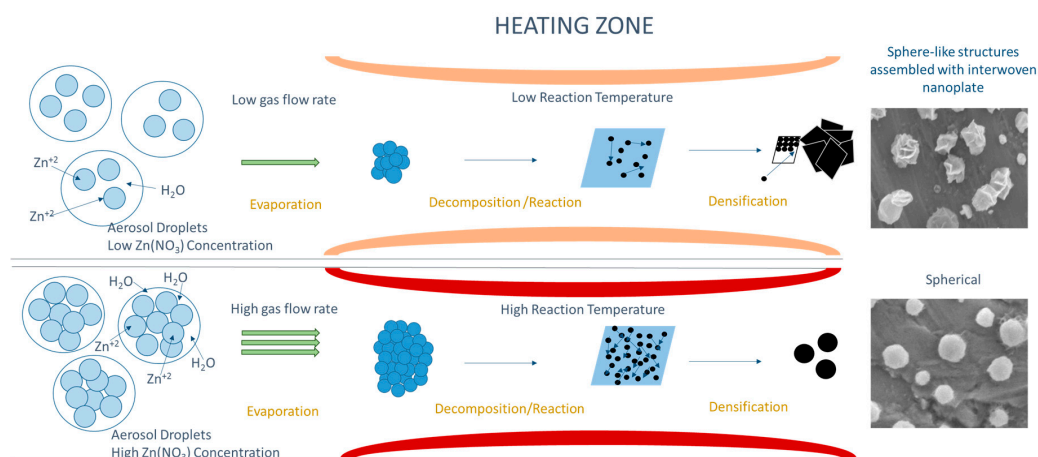


Figure 7. Schematic diagram of spherical and sphere-like structures assembled with interwoven nanoplate ZnO formation through Ultrasonic Spray Pyrolysis (USP).

Keeping in mind that morphological features of nanostructured ZnO particles are directly related to their functional properties, USP can be utilized as a suitable method targeting various application areas of ZnO. It has already been reported that higher surface areas of ZnO plates are favorable in photocatalysis applications [24]. For such applications, a synthesis strategy can be utilized dealing with low concentrations, temperatures and flow rates. On the other hand, the photocatalysis application necessitates the sintering of particles and UV-blockage properties, as spherical particles are more favorable owing to their good sinterability and good absorbance with less scattering of light [25,26]. For such applications, USP should be utilized at higher concentrations, temperatures and flow rates. A basic and empirical model can be found in Figure 7, which summarizes recipes to synthesize spherical or planar ZnO particles using the USP method.

4. Conclusions

The synthesis of pure and nanostructured ZnO particles was accomplished by USP. A lower concentration of $\text{Zn}(\text{NO}_3)_2 \cdot 6\text{H}_2\text{O}$ in the initial solution, and the reaction temperature and flow rate of N_2 resulted in lower Zn-saturation and, therefore, in lower nucleation rates. All these facts lead to the formation of nanostructured ZnO particles with a planar morphology, which is not typical for USP. Moreover, it was explained by the schematic representation of the formation mechanism, which showed that it is possible to control nanostructured ZnO particle morphologies, from spheres assembled by plates to plates via altering the USP parameters. This pioneering study aimed to explain the formation mechanisms of ZnO nanostructures and will contribute to targeting various applications in our next study.

Author Contributions: E.E., G.A., R.R., B.F. and designed the research, performed the experiments and analysed the data. D.J. provided the analysis tools and performed the characterisation. G.A., E.E. and R.R. wrote the article.

Acknowledgments: The authors would like to thank Gültekin GÖLLER and Technician Hüseyin SEZER for the SEM studies. The authors acknowledge the financial support from the Slovenian Research Agency (Research Core Funding No. P2-0120, P2-0132, BI-DE/17-19-12). The responsible proof reader for the English language is Shelagh Hedges, Faculty of Mechanical Engineering, University of Maribor, Slovenia.

Conflicts of Interest: The authors declare no conflict of interest.

Abbreviations

Ag	Silver
BF	Bright-Field
DS	Debye-Scherrer method
FE	SEM-Field Emission Scanning Electron Microscopy
HRTEM	High Resolution Transmission Electron Microscopy
N ₂	nitrogen
OH ⁻	Hydroxide ion
SAED	Selected Area Electron Diffraction
SEM	Scanning Electron Microscopy
UDM	Uniform Deformation Model
UV	Ultraviolet
USP	Ultrasonic Spray Pyrolysis
ZnO	Nanostructured zinc oxide particles
XRD	X-ray diffraction analysis
W-H	Williamson-Hall analysis

References

1. Yang, F.; Liu, W.H.; Wang, X.W.; Zheng, J.; Shi, R.Y.; Zhao, H.; Yang, H.Q. Controllable low temperature vapor-solid growth and hexagonal disk enhanced field emission property of ZnO nanorod arrays and hexagonal nanodisk networks. *ACS Appl. Mater. Interfaces*, **2012**, *4*, 3852–3859. [[CrossRef](#)] [[PubMed](#)]
2. Ali, L.I.; El-Molla, S.A.; Ibrahim, M.M.; Mahmoud, H.R.; Naghmash, M.A. Effect of preparation methods and optical band gap of ZnO nanomaterials on photodegradation studies. *Opt. Mater.* **2016**, *58*, 484–490. [[CrossRef](#)]
3. Sun, Y.; Chen, L.; Bao, Y.; Zhang, Y.; Wang, J.; Fu, M.; Wu, J.; Ye, D. The Applications of Morphology Controlled ZnO in Catalysis. *Catalysts* **2016**, *6*, 188. [[CrossRef](#)]
4. Dedova, T.; Acik, I.O.; Krunks, M.; Mikli, V.; Volobujeva, O.; Mere, A. Effect of substrate morphology on the nucleation and growth of ZnO nanorods prepared by spray pyrolysis. *Thin Solid Films* **2012**, *520*, 4650–4653. [[CrossRef](#)]
5. Klubnua, S.; Suwanboon, S.; Amornpitoksuk, P. Effects of optical band gap energy, band tail energy and particle shape on photocatalytic activities of different ZnO nanostructures prepared by a hydrothermal method. *Opt. Mater.* **2016**, *53*, 134–141. [[CrossRef](#)]
6. Gu, C.; Huang, J.; Wu, Y.; Zhai, M.; Sun, Y.; Liu, J. Preparation of porous flower-like ZnO nanostructures and their gas-sensing property. *J. Alloys Compd.* **2011**, *509*, 4499–4504. [[CrossRef](#)]
7. Singh, N.K.; Shrivastava, S.; Rath, S.; Annapoorni, S. Optical and room temperature sensing properties of highly oxygen deficient flower-like ZnO nanostructures. *Appl. Surf. Sci.* **2010**, *257*, 1544–1549. [[CrossRef](#)]
8. Kennedy, O.W.; Coke, M.L.; White, E.R.; Shaffer, M.S.P.; Warburton, P.A. MBE growth and morphology control of ZnO nanobelts with polar axis perpendicular to growth direction. *Mater. Lett.* **2018**, *212*, 51–53. [[CrossRef](#)]
9. Ding, J.; Fang, X.; Yang, R.; Kan, B.; Li, X.; Yuan, N. Transformation of ZnO polycrystalline sheets into hexagon-like mesocrystalline ZnO rods (tubes) under ultrasonic vibration. *Nanoscale Res. Lett.* **2014**, *9*, 1–6. [[CrossRef](#)] [[PubMed](#)]
10. Mahdavi, R.; Ashraf Talesh, S.S. The effect of ultrasonic irradiation on the structure, morphology and photocatalytic performance of ZnO nanoparticles by sol-gel method. *Ultrason. Sonochem.* **2017**, *39*, 504–510. [[CrossRef](#)] [[PubMed](#)]
11. Wang, H.; Xie, J.; Yan, K.; Duan, M. Growth Mechanism of Different Morphologies of ZnO Crystals Prepared by Hydrothermal Method. *J. Mater. Sci. Technol.* **2011**, *27*, 153–158. [[CrossRef](#)]
12. Huang, J.; Xia, C.; Cao, L.; Zeng, X. Facile microwave hydrothermal synthesis of zinc oxide one-dimensional nanostructure with three-dimensional morphology. *Mater. Sci. Eng. B Solid-State Mater. Adv. Tec.* **2008**, *150*, 187–193. [[CrossRef](#)]

13. Htay, M.T.; Hashimoto, Y.; Ito, K. Growth of ZnO submicron single-crystalline platelets, wires, and rods by ultrasonic spray pyrolysis. *Jpn. J. Appl. Phys. Part 1 Regul. Pap. and Short Notes and Rev. Pap.* **2007**, *46*, 440–448. [[CrossRef](#)]
14. Kajbafvala, A.; Ghorbani, H.; Paravar, A.; Samberg, J.P.; Kajbafvala, E.; Sadrnezhaad, S.K. Effects of morphology on photocatalytic performance of Zinc oxide nanostructures synthesized by rapid microwave irradiation methods. *Superlattices Microstruct.* **2012**, *51*, 512–522. [[CrossRef](#)]
15. Sin, J.C.; Lam, S.M.; Lee, K.T.; Mohamed, A.R. Self-assembly fabrication of ZnO hierarchical micro/nanospheres for enhanced photocatalytic degradation of endocrine-disrupting chemicals. *Mater. Sci. Semicond. Process.* **2013**, *16*, 1542–1550. [[CrossRef](#)]
16. Li, J.; Zhao, T.; Shangguan, E.; Li, Y.; Li, L.; Wang, D.; Wang, M.; Chang, Z.; Li, Q. Enhancing the rate and cycling performance of spherical ZnO anode material for advanced zinc-nickel secondary batteries by combined in-situ doping and coating with carbon. *Electrochim. Acta* **2017**, *236*, 180–189. [[CrossRef](#)]
17. Muñoz-Fernandez, L.; Alkan, G.; Milošević, O.; Rabanal, M.E.; Friedrich, B. Synthesis and characterisation of spherical core-shell Ag/ZnO nanocomposites using single and two-steps ultrasonic spray pyrolysis (USP). *Catal. Today* **2017**. [[CrossRef](#)]
18. Hidayat, D.; Ogi, T.; Iskandar, F.; Okuyama, K. Single crystal ZnO:Al nanoparticles directly synthesized using low-pressure spray pyrolysis. *Mater. Sci. Eng. B Solid-State Mater. Adv. Technol.* **2008**, *151*, 231–237. [[CrossRef](#)]
19. Gurmen, S.; Ebin, B. Production and characterization of the nanostructured hollow iron oxide spheres and nanoparticles by aerosol route. *J. Alloys Compd.* **2010**, *492*, 585–589. [[CrossRef](#)]
20. Gurmen, S.; Guven, A.; Ebin, B.; Stopic, S.; Friedrich, B. Synthesis of nano-crystalline spherical cobalt-iron (Co-Fe) alloy particles by ultrasonic spray pyrolysis and hydrogen reduction. *J. Alloys Compd.* **2009**, *481*, 600–604. [[CrossRef](#)]
21. Lojpur, V.; Mancic, L.; Rabanal, M.E.; Dramicanin, M.D.; Tan, Z.; Hashishin, T.; Ohara, S.; Milosevic, O. Structural, morphological and luminescence properties of nanocrystalline up-converting Y_{1.89}Yb_{0.1}Er_{0.01}O₃ phosphor particles synthesized through aerosol route. *J. Alloys Compd.* **2013**, *580*, 584–591. [[CrossRef](#)]
22. Emil, E.; Gürmen, S.; Hall, W. Estimation of yttrium oxide microstructural parameters using the Williamson–Hall analysis. *Mater. Sci. Technol.* **2018**, *836*. [[CrossRef](#)]
23. Ebin, B.; Arig, E.; Özkal, B.; Gürmen, S. Production and characterization of ZnO nanoparticles and porous particles by ultrasonic spray pyrolysis using a zinc nitrate precursor. *Inter. J. Miner. Metall. Mater.* **2012**, *19*, 651–656. [[CrossRef](#)]
24. Yassitepe, E.; Yatmaz, H.C.; Öztürk, C.; Öztürk, K.; Duran, C. Photocatalytic efficiency of ZnO plates in degradation of azo dye solutions. *J. Photochem. Photobiol. A Chem.* **2008**, *198*, 1–6. [[CrossRef](#)]
25. Tartaj, P.; Tartaj, J. Preparation, characterization and sintering behavior of spherical iron oxide doped alumina particles. *Acta Mater.* **2002**, *50*, 5–12. [[CrossRef](#)]
26. Neamjan, N.; Sricharussin, W.; Threepopnatkul, P. Effect of various shapes of ZnO nanoparticles on cotton fabric via electrospinning for UV-blocking. *J. Nanosci. Nanotechnol.* **2012**, *12*, 525–530. [[CrossRef](#)] [[PubMed](#)]

